

# Noise-Robust Microwave Breast Imaging Applied to Multi-Frequency Contrast Source Inversion

Hiroki Sato and Shouhei Kidera , *Member, IEEE*

**Abstract**—Ultra-wideband (UWB) microwave quantitative imaging offers less-painful examination, where a significant dielectric contrast between the malignant tumor and normal tissue is exploited. However, there are some difficulties in providing an accurate dielectric profile of breast media. This is because additive noises severely contaminate scattered signals. In this study, we apply a post-processing multi-frequency integration scheme to contrast source inversion (CSI) data to suppress image fluctuations. These are caused by the additive noise expected in a UWB system, which is also applicable to other inversion schemes. To deal with the dispersive dielectric properties in the CSI scheme, we introduce a first-derivative model of the Debye dispersion model to compensate for the dispersive effect. The FDTD numerical validations, using realistic breast phantoms with dispersive properties, show that a multi-frequency integration scheme considerably upgrades noise-robustness in complex permittivity reconstruction tissues.

**Index Terms**—Microwave imaging, contrast source inversion, multi-frequency integration, breast tumor imaging.

## I. INTRODUCTION

**B**REAST tumor has been reported by several studies, including the World Cancer Research Fund, as one of most diagnosed and fatal cancers globally. In the breast tumor detection, X-ray mammography has some disadvantages, such as cell-harmful X-ray exposure or highly pressured measurement, which causes intolerable pain to patients. While magnetic resonance imaging (MRI) modalities provide higher spatial resolution images, they require large, expensive equipment and lengthy measurement times. Ultrasound detection has several merits such as portability and low cost, but performs poorly when differentiating cancer cells from fibro-glandular tissues, especially for women with dense breasts [1]. Conversely, microwave breast tumor detection (*i.e.*, microwave mammography) offers benefits, such as low cost, compactness, safety, and screenings, which are both frequent and less painful, thus enhancing the examination rate, particularly for young women, however it is hardly considered standard care.

Manuscript received June 14, 2020; revised August 24, 2020 and October 12, 2020; accepted November 25, 2020. Date of publication December 2, 2020; date of current version May 21, 2021. This work was supported by the MIC/SCOPE #162103102, and in part by Japanese Ministry of Internal Affairs and Communications (MIC) under Grant MIC/SCOPE #162103102. (*Corresponding author: Shouhei Kidera.*)

The authors are with the Graduate School of Informatics, University of Electrocommunications Faculty of Informatics and Engineering Graduate School of Informatics and Engineering, Chofu 182-8585, Japan (e-mail: sato.hiroki@ems.cei.ucc.ac.jp; kidera@uoc.ac.jp).

Digital Object Identifier 10.1109/JERM.2020.3041592

The operating principle for microwave mammography is that there is a distinguishable dielectric contrast between normal and malignant breast tissues [2]. Reference [3], it was demonstrated that the dispersion property for each breast tissue is well-modeled by a single-pole Debye model at a lower microwave band. It is expected, though not yet clinically demonstrated, that an accurate profile of complex permittivity would contribute to a higher recognition rate in detecting malignant tumors. Microwave imaging is divided into radar and tomography-based approaches. As shown by several clinical tests [4]–[7], the radar based confocal approach has successfully localized cancer tissues within 10 mm [8]. However, if cancer tissues exhibit lower a contrast of dielectric property from the surrounding tissues, *e.g.*, fibro-glandular, then, the radar approach would perform poorly at discriminating cancerous tissues from other high-contrast tissues.

As a promising alternative approach, the tomographic scheme offers some advantages over radar-based methods, since a complex permittivity map is quantitatively reconstructed via inverse scattering analysis of the domain integral equation (DIE). The DIE's most critical issue is its solution to a non-linear, ill-posed problem. In such a case, Born approximation-based approaches, *e.g.*, and other approaches such as diffraction tomography [9] would not accurately reconstruct object profiles because of a large dielectric contrast from the background media. The distorted Born iterative method (DBIM), which is equivalent to the Gauss Newton method [10]–[13], has been demonstrated to accurately reconstruct dielectric profiles, including higher contrast cancer with dispersive media, by iteratively updating the background dielectric profile to avoid errors arising from non-linearity. While this approach requires fewer iteration steps, it requires computationally expensive solvers to update the Green's function and the total field within the region of interest (ROI) at each iterative step. Some other approaches to overcome the above difficulty have been investigated, *e.g.*, the level set approach [14], spatial prior [15], and deep neural network [16].

The contrast source inversion CSI method was developed by van den Berg *et al.*, [17] as a countermeasure to the DBIM. CSI iteratively updates the contrast source, the total electric field, and the object function in a sequential optimization scheme, as in [18]. A notable feature of CSI is that it does not require forward solvers if the Green's function of the background media is determined in closed form. Conversely, the numerical Green's function [19] or the partial differential equation (PDE)-based approach [20] is required in the case of an inhomogeneous background. The original CSI is based on single-frequency data,

and its reconstruction performance worsens severely even with a high signal-to-noise ratio (SNR) (e.g., 30 dB), which is relevant to actual scenarios [3]. In microwave breast imaging, the signal's strength is considerably attenuated by the lossy-dielectric property of biological tissues (e.g. skin and fibro-glandular). Therefore, the noise reduction scheme is crucial in distinguishing the attenuated signal from cancer.

This study focuses on a multi-frequency integration scheme to enhance the noise robustness of CSI's reconstruction performance. Several multiple frequency integration schemes, such as frequency hopping, have been introduced [21]. In these schemes, the initial guess achieved by a lower frequency response is used at a higher frequency iteration step. Reference [22] considered multi-frequency integrated CSI, but it did not deal with frequency dependent dispersive media, while a number of studies of multi-frequency CSIs have demonstrated that this technique is effective in producing more stable, accurate inversions [23], [24]. Few studies have focused on the biological media in multi-frequency CSI schemes like those of [25], in which the frequency-dependent dielectric property should be considered in using wideband microwave signals for breast cancer detection.

Based on the above background, this study introduces a novel multi-frequency integration CSI algorithm suitable for dispersive breast media. The basic idea behind the algorithm was proposed in [26], but that study did not mention or assess the noise-robustness features of multi-frequency integration scheme, which is the distinct focus of this paper. In the proposed method, a complex dielectric profile is reconstructed at each frequency using conventional CSI. The frequency-dependent parameter is then sequentially determined through weighted least squares on the single Debye model, acceptable for the most simple, appropriate and straightforward dispersion models of real breast tissues [2]. Finally, the proposed algorithm uses a post-processing scheme to integrate multiple results using the Debye formula's differentiation model to compensate for the frequency dependence. A notable advantage of the proposed method is that it considerably enhances the noise-robustness of the reconstruction results compared with that obtained from a single frequency-based CSI method. Our previous study [26] did not discuss or demonstrate that this advantage is achieved by coherently averaging the complex permittivity in a way that considers frequency-dependent variation. In addition, since our method is not based on a multi-frequency inversion scheme linked to a specific dispersion model, it could be extended to any dispersive model, drawing on the formula used to integrate the reconstruction results, and could be applied to other inversion schemes. The numerical tests by the two-dimensional (2-D) FDTD analysis, using an MRI-derived realistic breast phantom, verify that the proposed integration scheme significantly enhances the noise-robustness for various breast classes and across a range of SNR levels.

## II. CONTRAST SOURCE INVERSION (CSI)

### A. Observation Model

Fig. 1 shows array configuration, consisting of breast object comprising of adipose, skin, fibro-glandular, and cancerous

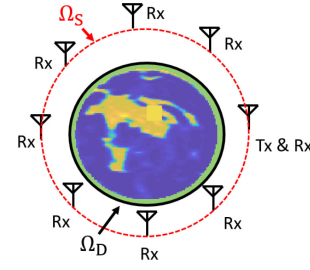


Fig. 1. System configuration. Breast media is included within the ROI as  $\Omega_D$ . Transmitters and receivers are located in domain  $\Omega_S$ .

tissues with dispersive dielectric properties. Multiple transmitters and receivers are arranged along the circumference of the breast, denoted as  $\Omega_S$ . The electro-magnetic wave is sequentially illuminated from a transmitting antenna, and is recorded in all receivers.  $\mathbf{r}_t$  and  $\mathbf{r}_r$  denote locations of the transmitters and receivers, respectively.  $E^{\text{total}}(\mathbf{r}_t, \mathbf{r}_r; f)$  is defined as the total electric field at the antenna combination of  $\mathbf{r}_t$  and  $\mathbf{r}_r$ , at specific frequency  $f$ .

### B. Forward Problem

The scattered electric field in observation domain  $\Omega_S$  is formulated by the Helmholtz type DIE as

$$\begin{aligned} E^{\text{scat}}(\mathbf{r}_t, \mathbf{r}_r, f) &\equiv E^{\text{total}}(\mathbf{r}_t, \mathbf{r}_r, f) - E^{\text{in}}(\mathbf{r}_t, \mathbf{r}_r, f) \\ &= k_b^2 \int_{\Omega_D} G_b(\mathbf{r}_r, \mathbf{r}, f) \chi(\mathbf{r}, f) E^{\text{total}}(\mathbf{r}_t, \mathbf{r}, f) d\mathbf{r}, \end{aligned} \quad (1)$$

where  $f$  denotes the frequency,  $\Omega_D$  denotes the ROI,  $E^{\text{total}}(\mathbf{r}_t, \mathbf{r}_r, f)$  is the total field,  $E^{\text{in}}(\mathbf{r}_t, \mathbf{r}_r, f)$  is the incident field,  $k_b$  denotes the background's wavenumber,  $\mu$  denotes the permeability, and  $G_b(\mathbf{r}_r, \mathbf{r}, f)$  denotes the Green's function of the background, which forms the zero-order Hankel function of the second kind. The contrast function, namely the object function, is denoted as  $\chi(\mathbf{r}, f) \equiv \epsilon(\mathbf{r}, f)/\epsilon_b(\mathbf{r}, f) - 1$ . Note that, if a background media is position independent (homogeneous) media, its Green's function is given by the closed form as the zero-th order Hankel function of the second kind. As a notable point of the CSI algorithm, the dummy variable, e.g., contrast source is defined as  $w(\mathbf{r}, f) \equiv E^{\text{total}}(\mathbf{r}_t, \mathbf{r}, f) \chi(\mathbf{r}, f)$ . Eq. (1) can then be reformulated as:

$$E^{\text{scat}}(\mathbf{r}_t, \mathbf{r}_r, f) = k_b^2 \int_{\Omega_D} G_b(\mathbf{r}_r, \mathbf{r}, f) w(\mathbf{r}, f) d\mathbf{r}, \quad (2)$$

The contrast source can also be expressed as:

$$\begin{aligned} w(\mathbf{r}, f) &= \chi(\mathbf{r}, f) E^{\text{in}}(\mathbf{r}_t, \mathbf{r}', f) \\ &+ \chi(\mathbf{r}, f) k_b^2 \int_{\Omega_D} G_b(\mathbf{r}', \mathbf{r}, f) w(\mathbf{r}, f) d\mathbf{r}, \quad (\mathbf{r} \in \Omega_D), \end{aligned} \quad (3)$$

The following notations in Eqs. (2) and (3) are defined as:

$$G^S w(\mathbf{r}_t, f) \equiv k_b^2 \int_{\Omega_D} G_b(\mathbf{r}_r, \mathbf{r}, f) w(\mathbf{r}, f) d\mathbf{r}, \quad (\mathbf{r}_t \in \Omega_S), \quad (4)$$

$$G^D w(\mathbf{r}, f) \equiv k_b^2 \int_{\Omega_D} G_b(\mathbf{r}', \mathbf{r}, f) w(\mathbf{r}, f) d\mathbf{r}, \quad (\mathbf{r} \in \Omega_D). \quad (5)$$

where subscripts  $S$  and  $D$  denote the domains of  $\Omega_S$  and  $\Omega_D$ , respectively. Eqs. (2) and (3) are called data equation and state (or object) equation, respectively.

### C. Inversion Algorithm

The original CSI algorithm solves  $\chi(\mathbf{r}, f)$  by minimizing the following cost function: Eq. (6), shown at the bottom of this page, where  $\|\cdot\|_S^2$  and  $\|\cdot\|_D^2$  are the  $l_2$  norms defined as the  $\Omega_S$  and  $\Omega_D$  domains, respectively. In the minimization process of  $F(\chi, w)$ , the variables  $w(\mathbf{r}, f)$ ,  $E^{\text{total}}(\mathbf{r}_t, \mathbf{r}, f)$ , and  $\chi(\mathbf{r}, f)$  are sequentially updated (see detail in [17]).

## III. MULTI-FREQUENCY INTEGRATION ALGORITHM

Several studies [21] have shown that multi-frequency strategies, such as the frequency hopping scheme, can enhance the reconstruction accuracy of the CSI method. Contrarily, there are few multi-frequency CSI studies have focused on dispersive media or objects, particularly the dispersive breast tumor detection scenarios. Specifically, the conventional CSI method [22] only considers the frequency dependency arising from the conductivity  $\sigma_s$  denoted as:  $\epsilon_r(f; \epsilon_\infty, \sigma_s) = \epsilon_\infty + \frac{\sigma_s}{j2\pi f \epsilon_0}$ , where  $\epsilon_\infty$  is the relative complex permittivity at infinite frequency. The literature [2] has demonstrated that the dielectric property of breast tissues (e.g., adipose, fibro-glandular, skin and tumor) is well modeled by the following single-pole Debye model:

$$\epsilon_{\text{Debye}}(f; \epsilon_\infty, \Delta\epsilon, \sigma_s) = \epsilon_\infty + \frac{\Delta\epsilon}{1 + j2\pi f\tau} + \frac{\sigma_s}{j2\pi f \epsilon_0}, \quad (7)$$

where  $\Delta\epsilon$  denotes the difference from  $\epsilon_\infty$  to the relative permittivity at zero frequency, and  $\tau$  is the relaxation time.

Previous studies [13] of multi-frequency integration required a specific dielectric property model according to a specific updating algorithm. To construct a method free from this limitation, this paper introduces a post-processing-based frequency integration scheme that is essentially applicable to various frequency-dependent models. To achieve appropriate integration using the numerical results from single-frequency CSIs, this study initially optimizes the Debye parameters from several single-frequency CSI results by weighted least squares minimization as

$$\begin{aligned} & (\hat{\epsilon}_\infty, \Delta\hat{\epsilon}, \hat{\sigma}_s) \\ & = \arg \min_{(\epsilon_\infty, \Delta\epsilon, \sigma_s)} \sum_{i=1}^{N_f} \xi_i |\epsilon_{\text{Debye}}(f_i; \epsilon_\infty, \Delta\epsilon, \sigma_s) - \tilde{\epsilon}^{\text{init}}(f_i)|^2. \end{aligned} \quad (8)$$

Here,  $\tilde{\epsilon}^{\text{init}}(f_i)$  denotes CSI's reconstruction profile using single frequency at  $f_i$ , at which the iteration steps are completed.  $N_f$  is the number of angular frequency bins and  $\xi_i \equiv \bar{E}^{\text{scat}}(f_i)$ ,

where  $\bar{E}^{\text{scat}}(f_i)$  denotes the norm of the complex valued scattered data of each frequency  $f_i$  via the Fourier transform, at a specific combination of  $\mathbf{r}_t$  and  $\mathbf{r}_r$ . The above weighting scheme, not considered in [26], is equivalent to the matched filtering approach, which is a maximally noise-robust filter.

By focusing on reconstruction at specific frequency  $f_i$ , the object function is updated by all other frequencies as:

$$\hat{\epsilon}(f_i) = \frac{\sum_{j=1}^{N_f} \xi_j \exp\left(\frac{-(f_i - f_j)^2}{2\sigma_f^2}\right) \tilde{\epsilon}(f_i; f_j)}{\sum_{j=1}^{N_f} \xi_j \exp\left(\frac{-(f_i - f_j)^2}{2\sigma_f^2}\right)}, \quad (9)$$

where  $\sigma_f$  denotes the correlation length for the multi-frequency integration, and  $\tilde{\epsilon}(f_i; f_j)$  is modeled using a first order approximation in Taylor expansion;

$$\tilde{\epsilon}(f_i; f_j) \equiv \tilde{\epsilon}^{\text{init}}(f_j) + \left. \frac{\partial \epsilon_r}{\partial f} \right|_{f=f_j} (f_i - f_j), \quad (10)$$

where  $\frac{\partial \epsilon_r}{\partial f}$  is defined as:

$$\frac{\partial \epsilon_r}{\partial f} = -\frac{j2\pi\tau\Delta\hat{\epsilon}}{(1 + j2\pi f\tau)^2} - \frac{\hat{\sigma}_s}{j2\pi f^2 \epsilon_0}. \quad (11)$$

According to the above expansion, the proposed method integrates multi-frequency CSI results for specific dispersive models appropriately. The above multi-frequency integration is expected to enhance reconstruction accuracy using the above averaging effect, especially in noisy scenarios. This method is often introduced to obtain an accurate complex permittivity profile at each frequency under noisy conditions. The simple Debye fitting scheme, using Eq. (8) only, could enhance noise-robustness by the averaging effect. However, the reconstruction result  $\hat{\epsilon}(f_i)$  using Eq. (9) still contains the information from initial reconstruction result  $\tilde{\epsilon}^{\text{init}}$  at each frequency  $f_i$ , which would be more informative than that obtained by the simple Debye model with only three degrees of freedom. This method can be applied to any dispersion model, such as multi-pole Debye or Cole-Cole, by reformulating Eqs. (8) and (11), and would be effective in other single-frequency inversion schemes.

## IV. RESULTS FROM NUMERICAL SIMULATION

### A. Numerical Settings

This section describes the numerical tests. Numerical data were generated using the in-house 2-D FDTD code at the University of Wisconsin Madison Cross-Disciplinary Electromagnetics Laboratory, where a single-pole Debye model, with a relaxation time  $\tau$  of 15 ps, was implemented using a frequency dependent model. Three types of realistic numerical phantoms are introduced from [27], for which the spatial profile of each Debye parameter could be associated with the magnitudes of real MRI

$$\begin{aligned} F(\chi, w) \equiv & \frac{\sum_{\mathbf{r}_r \in \Omega_S} \|E^{\text{scat}}(\mathbf{r}_t, \mathbf{r}_r, f) - G^S w(\mathbf{r}, f)\|_{\Omega_S}^2}{\sum_{\mathbf{r}_r \in \Omega_S} \|E^{\text{scat}}(\mathbf{r}_t, \mathbf{r}_r, f)\|_{\Omega_S}^2} \\ & + \frac{\sum_{\mathbf{r}' \in \Omega_D} \|\chi(\mathbf{r}, f) E^{\text{in}}(\mathbf{r}_t, \mathbf{r}', f) - w(\mathbf{r}, f) + \chi(\mathbf{r}, f) G^D w(\mathbf{r}, f)\|_{\Omega_D}^2}{\sum_{\mathbf{r}' \in \Omega_D} \|\chi(\mathbf{r}, f) E^{\text{in}}(\mathbf{r}_t, \mathbf{r}', f)\|_{\Omega_D}^2} \end{aligned} \quad (6)$$

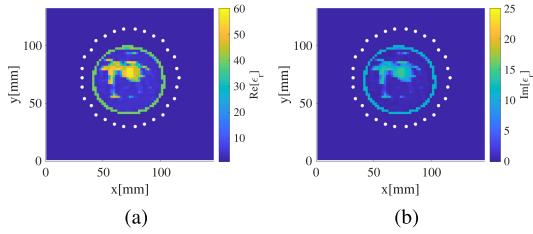


Fig. 2. Original profiles of complex permittivity [(a): real part and (b): imaginary part] of Class 3 at  $f = 2.01$  GHz. White solid circles denote source and observation points.

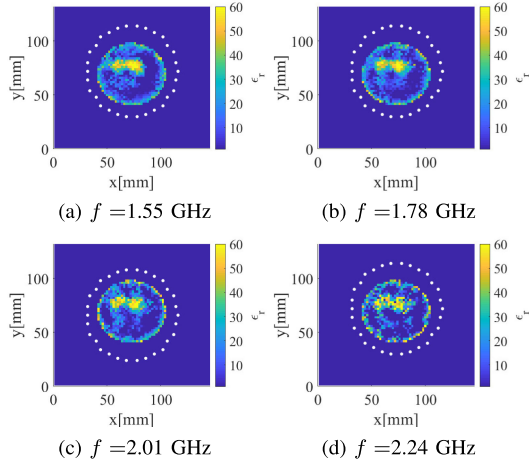


Fig. 3. Reconstruction results of the real part of complex permittivity at Class 3, using the CSI with the single frequency.

images [28]. A current forming a raised-cosine pulse modulated sinusoidal signal, with a center frequency of 2.0 GHz and a bandwidth of 2.1 GHz, was excited at each transmitting point. Thirty sets of source and observation points are located in the area surrounding the breast, and the  $S_{21}$  data of all combinations are processed. The cell size of FDTD and the unknown pixel are 2 mm. White Gaussian noise is added to each recorded total and incident electric field, as its relevance has been demonstrated in many studies [3], [29]. Here, the SNR is defined as the ratio of the maximum power of received signals to the average noise power. The maximal iteration number for CSI at each frequency is set to 30000, with no stopping condition applied.

### B. Case in Class3

At first, the representative case of Class 3 (heterogeneously dense) phantom with  $z = 16$  mm cross-section is investigated. Fig. 2 shows the original complex permittivity profile at 2.1 GHz frequency in this case, including 6-mm cancer cells with  $(\epsilon_{\infty}, \Delta\epsilon, \sigma_s) = (20.0, 38.0, \text{and } 0.8 \text{ S/m})$  [12] and fibro-glandular tissues with  $(\epsilon_{\infty}, \Delta\epsilon, \sigma_s) = (18.0, 31.0, \text{and } 0.75 \text{ S/m})$  on average. As a representative noisy scenario,  $\text{SNR} = 30$  dB is assumed. Figs. 3 and 4 show the reconstruction results by the original CSI method using a single frequency. It should be noted that we only investigated relatively low frequency data from 1.55 to 2.24 GHz of the received signal, which has a 2.0 GHz center frequency and 2.1 GHz bandwidth. This is because the accuracy of the

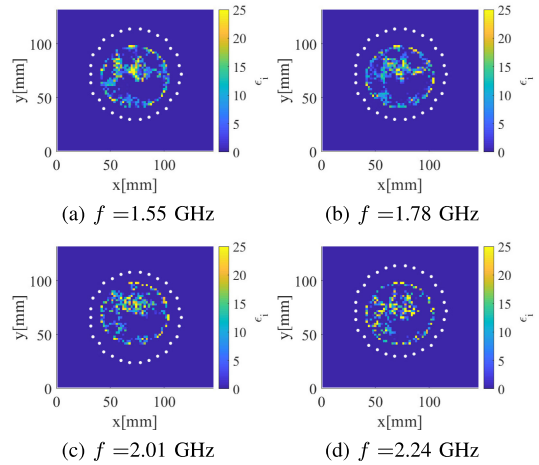


Fig. 4. Reconstruction results of the imaginary part of complex permittivity at Class 3, using the CSI with the single frequency.

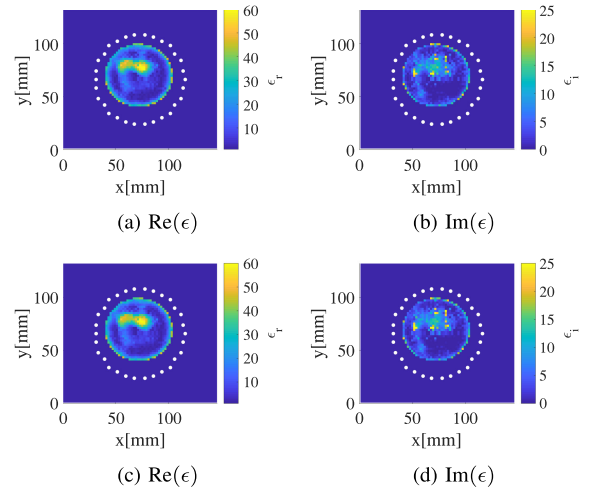


Fig. 5. Results of complex permittivity reconstruction at  $f = 2.01$  GHz by multi-frequency integrated CSI. (a) and (b):  $\sigma_f = 5\Delta f$ . (c) and (d):  $\sigma_f = 10\Delta f$ .

FDTD simulation should be guaranteed if the cell size (2mm) is smaller than  $1/10$  of the media wavelength. This condition is often violated for higher frequency data, particularly in cancer or fibroglandular tissues with higher relative permittivity. Complex permittivities at the lowest (1.55 GHz) and highest (2.24 GHz) frequencies are  $48.3 - 13.1i$  and  $47.6 - 12.3i$ , respectively, assuming the fibro-glandular tissue as  $(\epsilon_{\infty}, \Delta\epsilon, \sigma_s) = (18.0, 31.0, \text{and } 0.75 \text{ S/m})$  (see [2] more details). As shown in these figures, there are notable errors in each reconstruction due to random noise, even at relatively high SNR, and we need to consider the appropriate integration scheme for these results while also considering the frequency dependency. Fig. 5 shows the results of the proposed multi-frequency integrated CSI scheme at a frequency of 2.01 GHz, at which the two different cases of  $\sigma_f$  were tested. These results attest that our proposed method maintains reconstruction accuracy by suppressing the fluctuation of noise. As a quantitative criterion for error analysis, Fig. 6 shows the histogram of reconstruction errors for

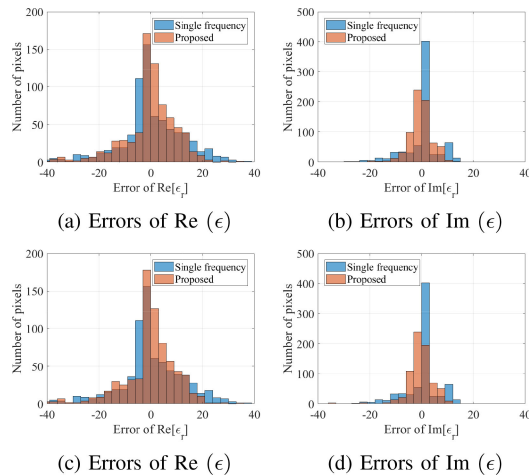


Fig. 6. Histogram of reconstruction errors at Class 3. (a) and (b): Case of  $\sigma_f = 5\Delta f$ . (c) and (d): Case of  $\sigma_f = 10\Delta f$ . Blue and red bars denote those of the single frequency and multi-frequency CSI, respectively.

TABLE I  
CUMULATIVE PROBABILITIES FOR EACH ERROR CRITERIA

	Error of $\text{Re}[\epsilon_r] \leq 5$	Error of $\text{Im}[\epsilon_r] \leq 5$
Single frequency ( $\sigma_f = 0$ )	48.2%	68.4%
Proposed ( $\sigma_f = 5\Delta f$ )	53.3%	76.8%
Proposed ( $\sigma_f = 10\Delta f$ )	53.0%	77.2%

TABLE II  
NRMSE IN COMPLEX PERMITTIVITY RECONSTRUCTION

	NRMSE of $\text{Re}[\epsilon_r]$	NRMSE of $\text{Im}[\epsilon_r]$
Single frequency ( $\sigma_f = 0$ )	0.219	0.507
Proposed ( $\sigma_f = 5\Delta f$ )	0.179	0.337
Proposed ( $\sigma_f = 10\Delta f$ )	0.179	0.374

both the real and imaginary parts of the complex permittivity. Table I and II also summarize the cumulative probabilities of reconstruction errors and normalized root mean square errors (NRMSE) in each method, respectively. These figure and tables quantitatively demonstrate remarkable improvement in reconstruction accuracy, achieved by appropriately compensating for the frequency dependency of the dispersive breast media. Note that the selection of  $\sigma_f$  naturally affects the reconstruction performance. A larger  $\sigma_f$  would cause an error because of the first order approximation of Taylor expansion in Eq. (10), and a smaller  $\sigma_f$  would result in a lack of noise-robust performance because of a lower averaging effect. We also confirmed that at least 5000 iterations are needed in each single frequency CSI to obtain similar reconstruction results at convergence. Not every per-iteration time is negligible in the 3-D model. Thus, we should shorten the iterations by using a more rapid convergence algorithm or introducing a suitable regularization term.

### C. Cases in Different Classes

To identify the relevance of our proposed method, other different types of classes as: Class 2 ‘‘Scattered Fibroglandula’’ and Class 4 (‘‘Very Dense’’) were used. Each Class has a different ratio of adipose to fibroglandular tissues. The left-side column in

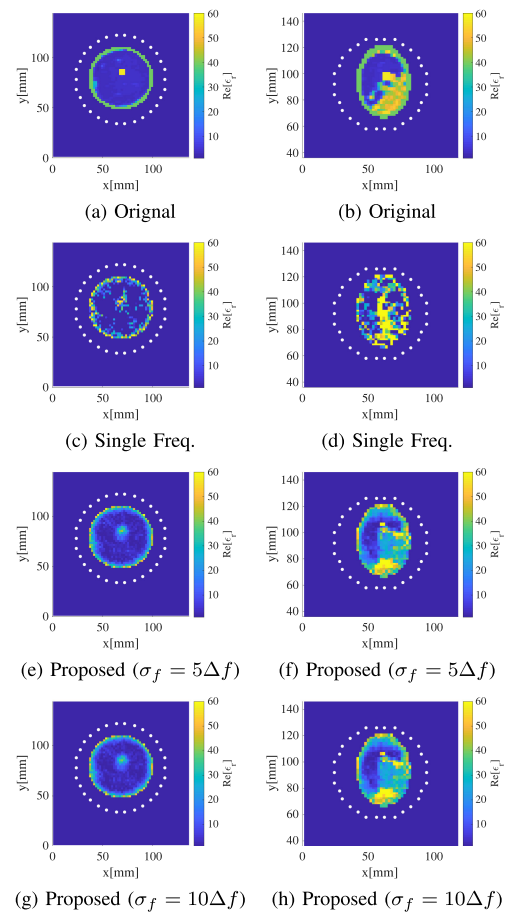


Fig. 7. Reconstruction results of for  $\text{Re}(\epsilon)$  at  $\text{SNR} = 30$  dB. (a),(c), (e), and (g): Class2, (b), (d), (f), and (h): Class4.

TABLE III  
MEDIAN VALUES OF NRMSES IN DIFFERENT SNRS

	$\text{Re}[\epsilon_r]$		$\text{Im}[\epsilon_r]$	
	Single Freq.	Multi Freq.	Single Freq.	Multi Freq.
0 dB	1.61	1.26	8.42	1.45
10 dB	1.43	0.85	8.23	1.36
20 dB	0.48	0.24	1.50	1.04
30 dB	0.23	0.17	0.53	0.32

Figs. 7 and 8 show the original profiles of relative complex permittivity for each class’s breast phantom at 2.01 GHz, including 6 mm size cancer tissues, with the same dielectric parameters as in Class 3. We also tested a representative case with an SNR of 30 dB, and investigated multiple frequencies with same range and intervals in the previous section. The middle and right columns in Figs. 7 and 8, show the reconstruction results, using the single frequency and multi frequency CSI (proposed method), respectively, where  $\sigma_f = 5\Delta f$  and  $\sigma_f = 10\Delta f$  are selected. These results demonstrate that our multi-frequency integration scheme is more effective than the single frequency CSI scheme, being similar to the case in Class 3. Table IV summarizes the quantitative error analysis using the normalized root mean square errors (NRMSE) in each class. These tables quantitatively demonstrate that there was significant improvement in the reconstruction accuracy, which was achieved by appropriately

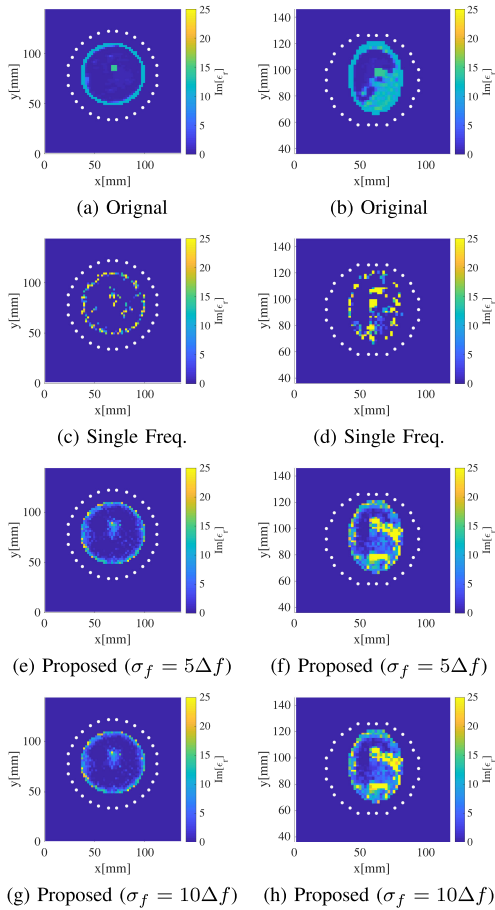


Fig. 8. Reconstruction results for  $\text{Im}(\epsilon)$  at  $\text{SNR} = 30$  dB. (a),(c), (e), and (g): Class2, (b), (d), (f), and (h): Class4.

TABLE IV  
NRMSEs IN DIFFERENT CLASSES AT  $\text{SNR} = 30$  dB

	Class 2		Class 3		Class 4	
	$\text{Re}[\epsilon_r]$	$\text{Im}[\epsilon_r]$	$\text{Re}[\epsilon_r]$	$\text{Im}[\epsilon_r]$	$\text{Re}[\epsilon_r]$	$\text{Im}[\epsilon_r]$
Single Freq.	0.244	0.541	0.245	0.533	0.754	1.89
Proposed $\sigma_f = 5\Delta f$	0.130	0.217	0.175	0.307	0.275	1.07
Proposed $\sigma_f = 10\Delta f$	0.128	0.223	0.175	0.328	0.263	1.17

compensating for the frequency dependency of the dispersive breast media. The above results barely confirm the dependency of correlation length ( $\sigma_f$ ). This dependency attests to the validity of first-order approximation in Eq. (11).

#### D. Statistical Error Analysis for Different SNR Cases

A statistical error analysis was performed with Class 3. We tested 20 different additive noise patterns at different SNR levels at 0, 10, 20, and 30 dB. Fig. 9 shows the box plot for the NRMSEs at each SNR level and demonstrates that the multi-frequency scheme in both cases of  $\sigma_f = 5\Delta f$  and  $\sigma_f = 10\Delta f$  considerably reduces the error divergence, especially at lower SNR levels *e.g.*, 0 dB or 10 dB. The lower and upper bounds of the boxes denote the interquartile range (IQR), and the lower and upper whiskers show the  $\pm 2.7$  standard deviation range. Table III also summarizes the median values of NRMSEs in different SNRs,

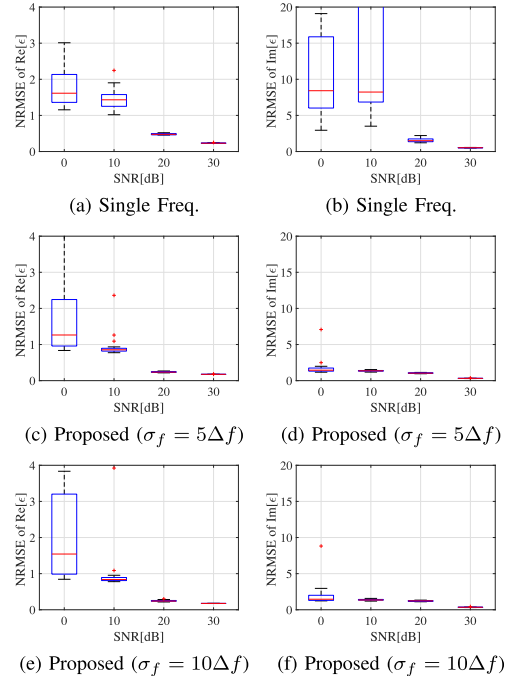


Fig. 9. Box plots of NRMSEs versus SNR with 20 different noise patterns in Class 3. (a), (c), and (e) : NRMSE of  $\text{Re}[\epsilon]$ . (b), (d), and (f): NRMSE of  $\text{Im}[\epsilon]$ . Red line shows the median value. The upper and lower band of the box denotes the first and third quartile, respectively.

and shows a significant improvement, in noise-robustness when using our proposed frequency integration scheme.

## V. CONCLUSION

This study introduced a noise-robust CSI method for dispersive breast media in which multiple frequency results were integrated via differentiation of the Debye formula. Numerical simulation combined with realistic breast phantoms, using various classes and SNR levels, demonstrated that our proposed algorithm significantly enhanced the noise-robustness, thereby improving CSI reconstruction performance. While the proposed method aimed to obtain more accurate reconstruction results at each single frequency using the specific Debye model, we noted that the recovered result  $\hat{\epsilon}(f_i)$  at each frequency  $f_i$  continues to contain the initial reconstruction information. This means that the whole results could be expressed as  $2N_f$  degrees of freedom at each cell, which the simple Debye fitting scheme would not yield. Also, this post-processing scheme could be applicable to other single frequency inversions. This information is particularly informative in a real-world scenario. This is because the real breast media do not always obey *a priori* specific dispersion model. Notably, the proposed noise reduction scheme is based on post-processing for several CSI results at each frequency. The Fourier transform conversion offers a certain de-noising level at pre-processing, by reducing the higher frequency noise component. Accordingly, a more advanced pre-processing de-noising approach like singular value decomposition [30] or wavelet analysis [31], is expected to offer even more noise-robust results. Note that a cell size in both the forward and inverse problem is precisely the same (*i.e.*, 2 mm), which may be viewed as

an inverse crime situation, meaning that the inversion model exactly represents the scattering target. Thus, an off-grid or smaller cell in the inversion scheme can better simulate real data. Such evaluations serve to recommend future research directions. Although the sensitivity or specificity rates are crucial criteria from the medical perspective, these rates are expected to depend strongly on selected recognition or feature extraction methods. Nevertheless, more accurate reconstruction profiles are expected to offer higher recognition rates. Future work can effectively explore this question.

## REFERENCES

- [1] G. A. G. M. Hendriks, C. Chen, H. H. G. Hansen, and C. L. de Korte, "3-D single breath-hold shear strain estimation for improved breast lesion detection and classification in automated volumetric ultrasound scanners," *IEEE Trans. Ultrasonics, Ferroelect., Freq. Control*, Vol. 65, no. 9, pp. 1590–1599, Sep. 2018.
- [2] M. Lazebnik *et al.*, "A large-scale study of the ultrawideband microwave dielectric properties of normal, benign, and malignant breast tissues obtained from cancer surgeries," *Phys. Med. Biol.*, vol. 52, pp. 6093–6115, 2007.
- [3] J. D. Shea, P. Kosmas, B. D. Van Veen, and S. C. Hagness, "Contrast-enhanced microwave imaging of breast tumors: A computational study using 3-D realistic numerical phantoms," *Inverse Probl.*, vol. 26, no. 7, Jul. 2010, Art. no. 74009.
- [4] P. M. Meaney, M. W. Fanning, Dun Li, S. P. Poplack, and K. D. Paulsen, "A clinical prototype for active microwave imaging of the breast," *IEEE Trans. Microw. Theory Techn.*, vol. 48, no. 11, pp. 1841–1853, Nov. 2000.
- [5] S. P. Poplack *et al.*, "Electromagnetic breast imaging: Results of a pilot study in women with abnormal mammograms," *Radiology*, vol. 243, no. 2, pp. 350–359, 2007.
- [6] E. C. Fear, J. Bourqui, C. Curtis, D. Mew, B. Docktor, and C. Romano, "Microwave breast imaging with a monostatic radar-based system: A study of application to patients," *IEEE Trans. Microw. Theory Techn.*, vol. 61, no. 5, pp. 2119–2128, May 2013.
- [7] E. Porter, M. Coates, and M. Popovic, "An early clinical study of time-domain microwave radar for breast health monitoring," *IEEE Trans. Biomed. Eng.*, vol. 63, no. 3, pp. 530–539, Mar. 2016.
- [8] E. J. Bond, Xu Li, S. C. Hagness, and B. D. Van Veen, "Microwave imaging via space-time beamforming for early detection of breast cancer," *IEEE Trans. Antennas Propag.*, vol. 1, no. 8, pp. 1690–1705, Aug. 2003.
- [9] P. Muller, M. Schurmann, and J. Guck, "The theory of diffraction tomography," Oct. 2016, *arXiv:1507.00466v3*.
- [10] J. Nocedal and J. J. Wright, *Nonlinear Optimization*, 2nd ed. New York, NY, USA: Springer, 2006.
- [11] P. M. Meaney, S. D. Geimer, and K. D. Paulsen, "Two-step inversion with a logarithmic transformation for microwave breast imaging," *Med. Phys.* vol. 44, no. 8, pp. 4239–4251, Aug. 2017.
- [12] D. W. Winters, B. D. Van Veen, and S. C. Hagness, "A sparsity regularization approach to the electromagnetic inverse scattering problem," *IEEE Trans. Antennas Propag.*, vol. 58, no. 1, pp. 145–154, Jan. 2010.
- [13] K. Noritake and S. Kidera, "Boundary extraction enhanced distorted born iterative method for microwave mammography," *IEEE Antennas Wireless Propag. Lett.*, vol. 18, no. 4, pp. 776–780, Apr. 2019.
- [14] T. J. Colgan, S. C. Hagness, and B. D. Van Veen, "A 3D level set method for microwave breast imaging," *IEEE Trans. Biomed. Eng.*, vol. 62, no. 10, pp. 2526–2534, Oct. 2015.
- [15] L. M. Neira, B. D. Van Veen, and S. C. Hagness, "High-resolution microwave breast imaging using a 3-D inverse scattering algorithm with a variable-strength spatial prior constraint," *IEEE Trans. Antennas Propag.*, vol. 65, no. 11, pp. 6002–6014, Nov. 2017.
- [16] L. Li, L. G. Wang, F. L. Teixeira, C. Liu, A. Nehorai, and T. J. Cui, "DeepNIS: Deep neural network for nonlinear electromagnetic inverse scattering," *IEEE Trans. Antennas Propag.*, vol. 67, no. 3, pp. 1819–1825, Mar. 2019.
- [17] P. M. van den Berg and R. E. Kleinman, "Contrast source inversion method," *Inverse Problems*, vol. 13, pp. 1607–1620, 1997.
- [18] M. T. Bevacqua, G. G. Bellizzi, T. Isernia, and L. Crocco, "A method for effective permittivity and conductivity mapping of biological scenarios via segmented contrast source inversion," *Prog. Electromagn. Res.*, vol. 164, pp. 1–15, 2019.
- [19] A. Abubakar and P. M. Van Den Berg, "Iterative forward and inverse algorithms based on domain integral equations for three-dimensional electric and magnetic objects," *J. Comput. Phys.*, vol. 195, no. 1, Mar. 2004, pp. 236–262.
- [20] A. Zakaria, I. Jeffrey, J. LoVetri, and A. Zakaria, "Full-vectorial parallel finite-element contrast source inversion method," *Prog. Electromagn. Res.*, vol. 142, pp. 463–483, 2013.
- [21] S. Sun, B. J. Kooij, T. Jin, and A. Yarovoy, "Through-wall imaging by TE and TM hybrid polarization inversion based on FDFD and frequency hopping scheme," *IET Int. Radar Conf.*, 2015, pp. 1–4, doi: 10.1049/cp.2015.1313.
- [22] R. F. Bloemenkamp, A. Abubakar, and P. M. van den Berg, "Inversion of experimental multi-frequency data using the contrast source inversion method," *Inverse Probl.*, vol. 17, pp. 1611–1622, 2001.
- [23] M. Asefi, A. Zakaria, and J. LoVetri, "Microwave imaging using normal electric-field components inside metallic resonant chambers," *IEEE Trans. Microw. Theory Techn.*, vol. 65, no. 3, pp. 923–933, Mar. 2017.
- [24] N. Gedert, L. Sparling, J. LoVetri, and I. Jeffrey, "Frequency-weighting for multi-frequency electromagnetic source contrast inversion," in *Proc. Int. Workshop Comput., Electromagn., Mach. Intell.*, 2018, pp. 15–16.
- [25] S. C. Wang, J. Zhang, B. Q. Xu, and M. S. Tong, "Microwave imaging for dispersive dielectric objects by contrast source inversion method," in *Proc. IEEE Int. Symp. Antennas Propag.*, 2016, pp. 861–862.
- [26] H. Sato and S. Kidera, "Multi-frequency integration algorithm of contrast source inversion method for microwave breast tumor detection," in *IEEE Proc. 41st IEEE Int. Eng. Med. Biol. Conf.*, Jul. 2019.
- [27] UWCEM, "Numerical breast phantom repository," [Online]. Available: <https://uwcem.ece.wisc.edu/phantomRepository.html>
- [28] M. J. Burfeindt *et al.*, "MRI-derived 3D-printed breast phantom for microwave breast imaging validation," *IEEE Antennas Wireless Propag. Lett.*, vol. 11, pp. 1610–1613, 2012.
- [29] C. Gilmore *et al.*, "Microwave biomedical data inversion using the finite-difference contrast source inversion method," *IEEE Trans. Antennas Propag.*, vol. 57, no. 5, pp. 1528–1538, May 2009.
- [30] J. D. Shea, B. D. Van Veen, and S. C. Hagness, "A TSVD analysis of microwave inverse scattering for breast imaging," *IEEE Trans. Biomed. Eng.* vol. 59, no. 4, pp. 936–945, Apr. 2012.
- [31] H. Zhang, T. Arslan, and B. Flynn, "Wavelet de-noising based microwave imaging for brain cancer detection," in *Proc. Antennas Propag. Conf.*, Loughborough, 2013, pp. 482–485.



**Hiroki Sato** received the B.E. degree in advanced mechanical and electrical engineering from the National Institute of Technology, Kisarazu College, Chiba, Japan, in 2018, and the M.E. degree in informatics and communication engineering from the University of Electro-Communications, Tokyo, Japan, in 2020.



**Shouhei Kidera** (Member, IEEE) received the B.E. degree in electrical and electronic engineering from Kyoto University in 2003 and the M.I. Ph.D. degree in informatics from Kyoto University, Kyoto, Japan, in 2005 and 2007, respectively. He has been with the Graduate School of Informatics and Engineering, the University of Electro-Communications, Tokyo, Japan, since 2009, and is currently an Associate Professor. In 2016, he was with the Cross-Disciplinary Electromagnetics Laboratory, the University of Wisconsin Madison as the Visiting Researcher. From

2017 to 2021, he was a Principal Investigator with the PRESTO Program of Japan Science and Technology Agency. His current research interests include advanced radar signal processing or electromagnetic inverse scattering issue for ultra wideband three-dimensional sensor or bio-medical applications. He was the recipient of the 2012 Ando Incentive Prize for the Study of Electronics, the 2013 Young Scientist's Prize by the Japanese Minister of Education, Culture, Sports, Science and Technology (MEXT), and the 2014 Funai Achievement Award. He is a Member of the Institute of Electronics, Information, and Communication Engineers of Japan, the Institute of Electrical Engineering of Japan, and the Japan Society of Applied Physics.